JACS
JOURNAL OF THE AMERICAN CHEMICAL SOCIETY

ARTICLE

pubs.acs.org/JACS

Self-Assembly of an Optically Active Conjugated Oligoelectrolyte

Julia H. Ortony,[†,‡] Tirtha Chatterjee,[‡,⊥] Logan E. Garner,[‡] Arkadiusz Chworos,[†] Alexander Mikhailovsky,[†] Edward J. Kramer,[*,‡,§,#] and Guillermo C. Bazan[*,†]

[†]Department of Chemistry and Biochemistry, Center for Polymers and Organic Solids, [‡]Materials Research Laboratory, [§]Department of Materials, and [#]Department of Chemical Engineering, University of California, Santa Barbara, California 93106, United States

[⊥]Analytical Sciences, The Dow Chemical Company, Midland, Michigan 48667, United States

Supporting Information

ABSTRACT: Conjugated oligoelectrolytes are of emerging technological interest due to their recent function in the fabrication of optoelectronic devices, application in biosensors, and as species that facilitate transmembrane charge migration. Solubility in aqueous, or highly polar, solvents is important for many of these applications; however, there are few studies on how the self-assembly of conjugated oligoelectrolytes into multichromophore species influences linear and nonlinear optical properties. Here, we examine 1,4-bis(4′-(*N*,*N*-bis-(6″-(*N*,*N*,*N*-trimethylammonium)hexyl)amino)-styryl)benzene tetraiodide (DSBNI) in water, a conjugated oligoelectrolyte based on the distyrylbenzene framework. We find that DSBNI aggregation leads to increased fluorescence lifetimes, coupled with hypsochromic shifts, and larger two-photon absorption cross sections. Liquid atomic force microscopy (AFM) and cryogenic transmission electron microscopy (cryo-TEM) were used to image DSBNI aggregates and to confirm that the planar molecules stack to form nanocylinders above a critical aggregation concentration. Finally, small-angle neutron scattering (SANS) was used to quantify the aggregate dimensions *in situ*. Comparison of the results highlights that the hydrophilic mica surface used to image via liquid AFM and the high concentrations required for cryo-TEM facilitate the propagation of the cylinders into long fibers. SANS experiments are consistent with equivalent molecular packing geometry but lower aspect ratios. It is therefore possible to understand the evolution of optical properties as a function of concentration and aggregation and the general geometric features of the resulting supramolecular structures.

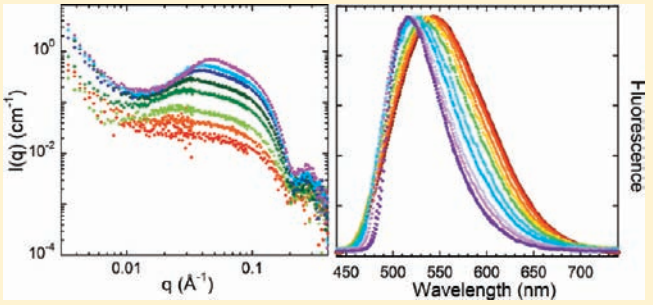

INTRODUCTION

Conjugated polyelectrolytes are defined by a π-delocalized backbone with pendant groups bearing ionic functionalities. Their oligomeric analogues, namely, conjugated oligoelectrolytes (COEs), are simpler to characterize and to use as study subjects for developing structure/property relationships due to their greater structural precision. The presence of the ionic component makes these materials unique, in that they combine the properties of organic semiconductors with the characteristics of polyelectrolytes.[1−4] For example, COEs exhibit solubility in aqueous environments and thereby may be incorporated as the light harvesting component of biosensory systems.[5−8] The efficiency of such systems, based on Förster resonant energy transfer (FRET), depends on relative interchromophore orientations and distances. Both of these parameters are mediated by the intermolecular interactions of the COEs in solution. More recently, amphiphilic COEs have been used to intercalate into the membranes of living microorganisms and thereby facilitate charge collection in microbial fuel cells. Controlling the supramolecular organization in these systems requires understanding the interplay between hydrophobic effects and electrostatic forces .[9]

The solubility of COEs in polar media has also been useful in the fabrication of multilayer optoelectronic devices via alternating the deposition of active layers from solvents of orthogonal polarity.[10] Furthermore, the ions in these materials are important in device function, as they can migrate and redistribute electric fields, or accumulate at metal/organic interfaces, and thereby reduce barriers to charge injection.[11,12] Film morphology influences the charge carrier and ion mobilities. Efforts to control film morphology have up until now focused on casting methods[13] but not on self-assembly of chromophores in the solution from which the devices are cast.

Figure 1 shows the chemical structure of 1,4-bis(4′-(*N*,*N*-bis-(6″-(*N*,*N*,*N*-trimethylammonium)hexyl)amino)-styryl)benzene tetraiodide (DSBNI). COEs of this type have served as subjects to probe how the two photon absorption (TPA) of organic chromophores changes as a function of structural modifications and solvent properties.[14] The optically active core in DSBNI contains a distyrylbenzene bridge with two donor substituents at

Received: March 28, 2011
Published: May 06, 2011

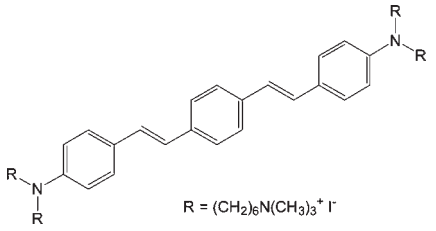

Figure 1. Molecular structure of DSBNI.

the α and ω positions and was chosen on the basis of established molecular guidelines to optimize the TPA cross section, δ.[15] By comparison against molecular counterparts that are neutral, but with isostructural optical cores, it was found that the effect of the solvent dielectric constant was nonmonotonic and that the δ value was highest in a solvent of medium polarity (tetrahydrofuran) and lowest in water.[16] Significantly, there was little correlation between experimental results and theoretical expectations.[17]

While examining DSBNI in water, we found unanticipated variations in the linear and two photon spectroscopies as a function of concentration. We show herein that these changes are due to the formation of supramolecular aggregates stabilized by hydrophobic interactions.[18] Such structures allow us to understand how self-assembly influences the local environment of π-delocalized molecular systems via the monitoring of relevant spectroscopic signatures. Because of the changes in local environment that result from aggregation of COEs, it may be possible to control self-assembly to tailor the distance and orientation of small-molecule organic semiconducting materials.[19−21] Detailed insight into the structural features of the DSBNI aggregates as a function of various environments is provided by using different characterization tools.

EXPERIMENTAL SECTION

Materials. DSBNI was synthesized as previously described.[16] All solutions were made using HPLC grade water. Samples used for fluorescence lifetime measurements and two photon absorption (TPA) cross-sectional measurements were degassed before the measurements were carried out. For SANS measurements, DSBNI aggregates were studied in D_2O (Cambridge Isotopes).

Spectroscopy. A Shimadzu UV-2401 spectrophotometer was used to capture absorbance spectra in quartz cuvettes. Photoluminescence (PL) spectra were captured using a Spex Fluorolog 2 spectrometer at a 90° detection angle.

Two-Photon Absorption. TPA cross section (δ) measurements were carried out in the UCSB Optical Characterization Facility. TPA-induced fluorescence excitation was achieved using a mode-locked Ti:sapphire laser (Spectra Physics Tsunami) operating with a repetition rate of 80 MHz and providing <6 nJ, 100 fs excitation pulses. Samples were excited with a tightly collimated (diameter ∼120 μm) laser beam and the up-converted fluorescence was detected at 90°. The emitted light from the sample was collected by a high numerical aperture lens and routed into a spectrometer (Acton SpectraPro-300) equipped with a thermoelectrically cooled CCD camera (Roper Scientific PIXIS:400). Near-infrared (NIR) excitation light was blocked by short-pass glass and interference filters. TPA-induced fluorescence was monitored over the range 400−750 nm.

For the quantitative determination of δ, we utilized TPA photoluminescence excitation technique.[16,22] The measurements of the integrated fluorescence intensity enabled us to determine the δ according to the equation[23]

$$\delta = \frac{\Phi_{ref}\delta_{ref}c_{ref}P_{ref}^2 I}{\Phi c P^2 I_{ref}}K \quad (1)$$

where index ref denotes values obtained in the reference sample under identical experimental conditions. A correction factor K is obtained from the refractive indices of solvents used to prepare the samples ($K = n^2/n_{ref}^2$), I and I_{ref} are the integrated fluorescence intensities, P and P_{ref} are the excitation powers employed, c and c_{ref} are the concentrations, and Φ and Φ_{ref} are the fluorescence quantum yields under single photon excitation for the sample and reference, respectively. The reference standard used was fluorescein dye (10 μM in aqueous solution at pH 11), the TPA spectra of which has been reported in the literature.[22]

Fluorescence Lifetimes. Fluorescence lifetime measurements were performed using Time-Correlated Single Photon Counting (TCSPC) technique.[24] Approximately 100 fs excitation pulses with wavelength 375 nm were generated by doubling the fundamental frequency of femtosecond Ti:Sapphire laser (Spectraphysics Tsunami) pulses in β-barium borate crystal. The laser repetition rate was reduced to 2 MHz by a homemade acousto-optical pulse picker in order to avoid saturation of the chromophore. The TCSPC system was equipped with an ultrafast microchannel plate photomultiplier tube detector (Hamamatsu R3809-U-51), and electronics correlator board (Becker & Hickl SPC-630), and has instrument response time less than 50 ps. A triggering signal for the TCSPC board was generated by sending a small fraction of the laser beam onto a fast (400 MHz bandwidth) Si photodiode (Thorlabs, Inc.). Fluorescence was dispersed in Acton Research SPC-300 monochromator after passing through a pump blocking, long wavelength-pass, autofluorescence-free, interference filter (Omega Filters, ALP series). The monochromator was equipped with a CCD camera (Roper Scientific PIXIS-400) allowing for monitoring of the fluorescence spectrum. Fluorescence transients were not deconvolved with the instrument response function since their characteristic time-constants were much longer than the width of the system response to the excitation pulse.

Liquid AFM. A MultiMode Atomic Force Microscope (Veeco, Santa Barbara, CA) equipped with a Nanoscope IIIA controller and E scanner was used to capture height images in tapping mode under solution. Gold-coated SiN cantilevers with spring constants of ∼0.01 N/m (MSCT-Au, Veeco Probes) were used at their peak resonant frequency of ∼8 kHz. Mica substrates were cleaved immediately before use, and solutions were given ∼1 h equilibration time on the substrates in the fluid cell before imaging.

Solution Conductance. An electrochemical cell was built to accommodate small volumes (∼100 μL) while maintaining a constant electrode surface area and a constant interelectrode distance. A bias was reversibly swept from −3 to 3 V at a scan rate of 1.87 V/s. Current−voltage curves were measured using a Keithley 2400 source meter.

Cryo-TEM. An FEI Tecnai G2 Sphera transmission electron microscope (operating voltage 200 kV) was used to obtain cryo-TEM images. Samples were deposited onto holey carbon grids, then were robotically blotted and injected into a liquid mixture of propane/ethane (60:40) for freezing. The TEM micrographs were taken using a Gatan Ultrascan 1000 CCD camera.

Small Angle Neutron Scattering. Small angle neutron scattering (SANS) measurements were conducted at the NIST Center for Neutron Research (NCNR), Gaithersburg, MD. The data were collected at 25 °C using the NG3 30-m SANS instrument with neutron wavelength (λ) 6 Å and $\Delta\lambda/\lambda$ = 11%. Three sample to detector distances, 1.3, 4.0, and 13.2 m, respectively, were used to cover a scattering vector q ($q = 4\pi/\lambda \sin(\theta/2)$, where λ and θ are the neutron wavelength and scattering angle, respectively) range of 0.0034−0.4 Å^{-1}. All measurements were done with samples loaded in quartz window with 1.0 mm gap assembled into a titanium cell with o-rings. The recorded

two-dimensional data were corrected for empty cell and parasitic background scattering. Further, the 2D data were reduced to one dimension (intensity vs q) using the software[25] available at NCNR, NIST, and placed on an absolute intensity scale (using an attenuated empty beam).

SANS Data Analysis. The SANS data were analyzed using model independent Guinier analysis and form-factor/structure-factor modeling. According to the Guinier approximation, the scattering intensity at low q is given by: $I(q) = I(0)\exp(-q^2R_g^2/3)$ where $I(0)$ is the extrapolated absolute intensity at $q = 0$ and R_g is the radius of gyration/characteristic length scale. Following this expression, the R_g values can be determined from the slope of a plot of $\ln[I(q)]$ versus q^2. For a two phase system, as in our case, the obtained characteristic length scale (R_g) represents an effective scattering domain size and is much bigger than the individual scattering objects. The Guinier analysis is independent of the absolute intensity and any model and typically valid for the low q region satisfying the condition $qR_g < \sqrt{3}$. However, instrumental smearing, polydispersity, and the interparticle interactions (structure factor) appear to decrease the effective R_g values. Especially, the influence of the structure factor at low q is generally significant for the charged polyelectrolytes. For this reason, the typical region used for the Guinier fit for such systems is given as: $1.3 < qR_g < 2.5$.[26] The qR_g range over which our data were fit was $1.7 < qR_g < 2.7$ which is slightly above where the Guinier approximation is expected to hold.

The SANS intensity data were also fit to a form-factor/structure-factor model of the form

$$I(q) = \phi(\Delta\rho)^2P(q)S(q) + I_{bgd} \quad (2)$$

where φ is the particle volume fraction (scaling factor), $P(q)$ and $S(q)$ are the form and structure factors, respectively, and I_{bgd} is the incoherent scattering background. $\Delta\rho$ is the scattering contrast which is essentially the difference in neutron scattering length density between DSBNI molecules and D_2O (solvent). For this study, a monodisperse rigid cylinder (length L and radius r) form factor was used which is normalized by the particle (cylinder) volume and given as:

$$P(q) = \frac{1}{V_{cyl}}\int_0^{\pi/2} f^2(q,\alpha)\sin\alpha d\alpha$$
$$f(q,\alpha) = 2V_{cyl}j_0\left(\frac{qL}{2}\cos\alpha\right)\frac{j_1(qr\sin\alpha)}{qr\sin\alpha} \quad (3)$$

where $V_{cyl} = \pi r^2L$, $j_0(x) = \sin(x)/x$ and $j_1(x) = [\sin(x)/x^2 - \cos(x)/x]$, respectively. '$\alpha$' is defined as the angle between the cylinder axis and the scattering vector q. The integral over α averages the form factor over all possible cylinder orientations. To accommodate interparticle scattering, the above-mentioned form factor was coupled with a structure factor based on a mean spherical approximation[27,28] which accounts for the electrostatic repulsion (screened Coulomb) between charged cylinders. This approximation has been widely used for different charged micelle structures.[26,29−31] This potential is applicable in the absence of angular correlation between the micelles, a reasonable assumption here, considering the low concentration oligoelectrolyte solutions studied. The fitting parameters related to this structure factor are the micelle effective charge (z_{eff}), micelle diameter, and volume fraction along with input values for the temperature (set to 298 K), monovalent salt concentration (set equal to critical aggregation concentration (CAC)), and solvent dielectric constant (78.0 for D_2O). The model fit was performed using the data analysis software available at NCNR, NIST.[25]

RESULTS AND DISCUSSION

Concentration-Dependent Optical Properties. The linear optical behavior of DSBNI in water as a function of concentration was initially examined by measuring the absorbance and emission spectra. The absorbance spectra for representative dilute (2.00 μM) and concentrated (3.00 mM) solutions are shown in Figure 2, and their corresponding molar absorption coefficients (ε_{max}) are presented in Table 1. The dilute solution exhibits an ε_{max} of 5.6×10^4 cm^{-1} M^{-1} with no vibronic fine structure. We observe a slightly lower ε_{max} of 5.0×10^4 cm^{-1} M^{-1} for the concentrated (3.00 mM) solution with a low energy shoulder in the absorption band.

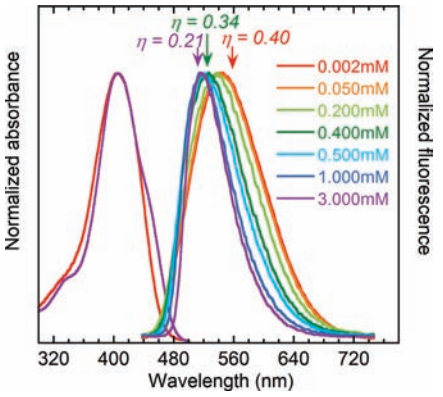

Figure 2. Linear absorption and fluorescence (excitation λ = 405 nm) spectra of aqueous DSBNI solutions.

Table 1. Summary of Optical Properties of DSBNI Solutions

[DSBNI][a]	λ_{PL} (nm)	ε (M^{-1} cm^{-1})	τ_{max} (ns)	η^b	δ_{max} (GM)
2.00 μM	550	5.6×10^4	1.35	0.40	525
3.00 mM	515	5.0×10^4	7.23	0.21	770

[a] DSBNI solutions were freshly prepared in pure water. [b] PL quantum yields determined using fluorescein pH 12 standard (2.00 μM), and an integrating sphere (3.00 mM).

Also shown in Figure 2 are the changes in the PL spectra of DSBNI, together with three corresponding PL quantum yields (η). When [DSNBI] = 2.00 μM, the emission maximum (λ_{PL}) occurs at 550 nm. Under these conditions, $\eta = 0.40$. No change in either η or λ_{PL} is observed at lower concentrations. As the concentration increases to 3.00 mM, one observes a blue shift from 550 to 515 nm. Simultaneously, the η value decreases by almost half (0.40 to 0.21). At the intermediate concentration of 0.400 mM, only a slight blue shift is observed (λ_{PL} = 525 nm) and $\eta = 0.34$. It is interesting to highlight at this junction that stronger DSBNI interactions would be expected at the highest concentrations. However, these conditions typically yield red-shifted emission spectra, as in the case of [2.2]paracyclophane bichromophoric systems that bring together two optical units similar to DSBNI.[32]

Fluorescence lifetime measurements were performed to examine the properties of the DSBNI excited state and the results of this study are shown in Figure 3. Under dilute conditions ([DSBNI] = 2.00 μM, shown in red), the intensity decay is characterized by a single exponential term with a lifetime (τ) of 1.3 ns. In the intermediate regime (0.400 mM, shown in green), the fluorescence lifetime increases and can no longer fit to a single exponential curve. The decay observed for a 3.00 mM solution reflects a considerably longer lifetime than as observed at more dilute conditions. The enhancement of fluorescence lifetime with increasing concentration is consistent with interchromophore electronic delocalization and suggests the formation of aggregates in solution.[33,34]

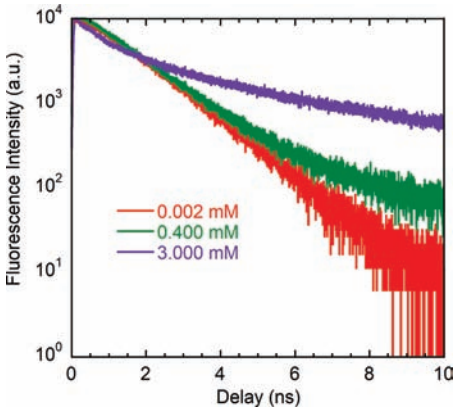

Figure 3. Fluorescence decay traces of aqueous DSBNI solutions. Lifetimes were measured from the maximum fluorescence wavelength of each solution.

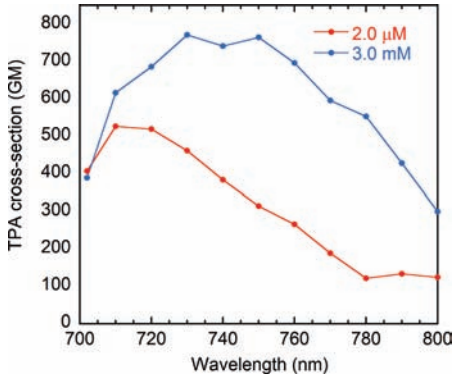

Figure 4. Two-photon absorption cross section of DSBNI solutions in water (GM = 10^{-50} cm^4 s photon^{-1}).

DSBNI and related chromophores exhibit two-photon absorption (TPA) spectra in which the magnitude of δ is sensitive to the medium.[14] In particular, distyrylbenzene derivatives have higher TPA cross sections in nonpolar solvents than in water.[16] Figure 4 shows the TPA spectra of DSBNI at the two extremes of the concentration range, as obtained via the two-photon excitation fluorescence technique, as described previously.[16] The TPA emission (not shown) is identical to that resulting from one photon excitation, indicating that the same excited state is accessed via the two processes. The 2.00 μM solution yields a maximum TPA cross section (δ_{max}) of 525 GM (GM = 10^{-50} cm^4 s photon^{-1}), whereas at 3.00 mM, a value of 770 GM is obtained. These results highlight the variability in TPA as a function of concentration and support the idea that the chromophore is surrounded by a less polar medium at the high concentration, as would be expected by closer DSBNI—DSBNI proximity.

Characterization of DSBNI Aggregates by Liquid-AFM and Cryo-TEM. Solution conductances as a function of [DSBNI] were measured to determine whether a distinct concentration exists at which aggregates form. This method is widely used for surfactant systems and yields the CAC from the point at which the slope changes in the plot of conductance as a function of concentration.[35] The slope of each current−voltage curve at a constant [DSBNI] provides the conductance of the corresponding solution, and this value is plotted against concentration, as

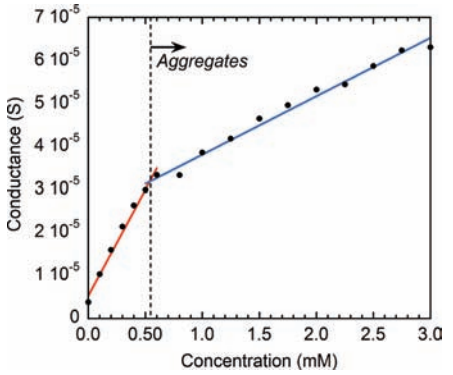

Figure 5. Change in conductance of DSBNI solutions.

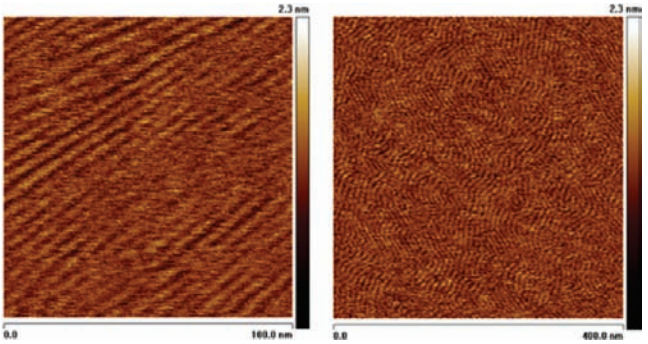

Figure 6. Liquid atomic force microscope height images of 1.5 mM DSBNI (aq) on mica.

shown in Figure 5. Two intersecting linear regimes are observed, which can be fit to obtain a slope of 67 μS mM^{-1} in the dilute regime and 14 μS mM^{-1} in the concentrated regime. These data imply that the onset of DSBNI aggregation occurs at 0.51 mM.

Figure 5 provides the limiting concentration at which DSBNI molecules come together and form supramolecular structures; however, these data do not yield quantitative information regarding the size and shape of the aggregates. To characterize the morphology and to gain insight into the internal structure of the aggregates, amplitude modulated liquid atomic force microscopy (liquid AFM) was used.[36] This technique has enabled observation of biological molecules in aqueous environments with nanoscale resolution.[37] We implemented this method by preparing a solution above the aggregation threshold concentration, and allowing it to equilibrate on freshly cleaved mica for 1 h under high relative humidity (the sample was suspended over a water/air interface of 18 cm^2 with a chamber volume of 50 mL). The sample was then transferred into the instrument where the DSBNI solution was injected into a fluid cell. A SiN probe with a gold-coated cantilever was used to image the surface in tapping mode under solution. Freshly cleaved mica has a very low surface roughness (<1 Å) and has interfacial potassium ions that dissociate to produce an anionic surface in aqueous solution. These traits allow the cationic DSBNI aggregates to adhere to the surface so that the aggregate/solution interface may be imaged. As shown in Figure 6, wormlike micelles are observed that retain some degree of order on the surface over a length scale of ~100 nm. Cross-sectional analyses show the average diameter of each structure to be 4.4 nm, with a height of 0.84 nm. The beginning and end of several micelles can be resolved in the AFM

Figure 7. Cryogenic transmission electron microscope (cryo-TEM) images of saturated DSBNI (aq) solution. Wormlike micelles with diameters of ~5 nm are observed.

images; thus, their lengths can be approximated as >400 nm under the experimental conditions described.

Analysis of the atomic force micrographs indicates that the cross section of the micelles is roughly elliptical, and that the elliptic major axis corresponds to the length of one DSBNI molecule (~3.6 nm). Differences between the measured cross-sectional shape of the micelles on mica and the molecular length may be a result of the spatial convolution of the AFM tip shape and the dimensions of the adsorbed aggregates. We also anticipate DSBNI to exhibit a circular cross section when averaged over the length of a micelle. According to this packing motif, the plane of each DSBNI molecule within the micelle is expected to be roughly perpendicular to the direction of micellar propagation.

Liquid atomic force micrographs provide information regarding the dimensions of aggregates in solution, but this technique requires an anionic substrate over which electrostatic forces may facilitate intermolecular or intermicellar interactions. To confirm the presence of cylindrical aggregates, while excluding surface effects, cryogenic transmission electron microscopy (cryo-TEM) measurements were carried out, and typical results are shown in Figure 7. No images of micelles were obtained using cryo-TEM except at very high concentration (saturated) in aqueous solution. Cryo-TEM of saturated DSBNI showed thread-like aggregates with a diameter of ~5 nm. The dimensions observed are consistent with those observed on the surface of mica using liquid AFM and further support the presence of self-assembled nanostructures in concentrated DSBNI solution.

SANS Characterization. SANS measurements were performed to examine the DSBNI structures truly in solution (not on mica as in Figure 6) at concentrations expected to exhibit aggregation but below the saturation threshold. This technique is widely used to study structural properties in solutions containing polymers,[38] micellar and microemulsion systems,[39] nanoparticles,[40,41] and biological macromolecules.[42] Figure 8a shows the SANS intensity profiles for different DSBNI concentrations in D_2O. As observed in these profiles, both the intermediate and high q scattering data display two distinct peaks. We anticipate that above the CAC, the intermolecular $\pi-\pi$ interactions guide DSBNI molecules to a self-aggregated structure. On a larger length scale, these structures interact (governed by the electrostatic repulsive force) with each other to form a correlation peak. On the basis of this assumption, we infer the high q peak arises from the micelle form factor, whereas the intermediate q peak is a manifestation of the average center to center distance between the aggregated structures. The slope of the scattering curve over the appropriate q-range is consistent with an expected q^{-1} at intermediate q values and q^{-4} at high q. Further, the low q region scattering data, for all concentrations studied here, display an upturn. This feature indicates that a larger length scale is associated with this system, and a simple power law analysis reveals a $q^{-2.4\pm0.4}$ relation, which is typical for a mass fractal system.

To verify our hypothesis about cylindrical DSBNI aggregates with a specific correlation length (ξ, the average center to center distance between cylindrical micelles), we fit the data using a form factor-structure factor model as described in the Experimental Section. The use of cylindrical form factor coupled with a structure factor,[27,28] accounting for the electrostatic repulsion, exhibits an excellent fit as presented in Figure 8b (solid black line). The deconvolution of a representative fit into corresponding form and structure factors is also displayed as an inset of Figure 8b. The extracted fitting parameters along with the quality of fitting are presented in Table 2. The radius of the aggregated cylinders was found to be 18 Å and is independent of the DSBNI concentration. This value is in agreement with the liquid AFM data (average radius found to be 22 Å using AFM). Interestingly, the optimized distance calculated (using AM1[43] level)[44] between two end nitrogen molecules connected through three *p*-phenylenevinylene groups is 18.82 Å. We estimate the radius of gyration of a DSBNI molecule to be approximately 35 Å. This value is fully consistent with the micelle diameters, and therefore indicates that the plane of the DSBNI chromophore is along the cylinder radial direction with each full DSBNI molecule spanning the diameter of the cylinder. Surprisingly, the length of the cylinder was found to be much shorter ~37 Å compared to that observed using liquid AFM and invariant for the concentration window examined through SANS measurements. The growth of the cylinder along the axial direction is governed by the $\pi-\pi$ stacking of DSBNI molecules. Presumably, the short-range interaction potential limits the aggregated cylinder growth along the axial direction. Conversely, during liquid AFM in the presence of an anionic mica surface, these shorter cylindrical structures seemingly ordered themselves into longer cylinders or worm like structures. In passing, we mention that to be confident with the formation of short cylinders, we further fitted the SANS data using a uniform ellipsoid form factor (and the same structure factor as described above). The comparison (structural length scales and fitting statistics) between these two models for every concentration showed that the cylindrical form factor model returned better statistics (see Supporting Information, S1 and S2).

Given that the cylinder dimension (where, length of the cylinder ≈ diameter of the cylinder ≈35−37 Å) for the concentration window presented in Figure 8, and the approximate R_g value of DSBNI molecule are in close proximity to both the cylinder length and diameter, we further investigated the structural assignment. According to the dimensions determined by SANS, the orientation of the DSBNI molecules in the cylinders can be of either orientation depicted in Figure 9 (with chromophores along the radial plane ("Cylinder A") or the axial

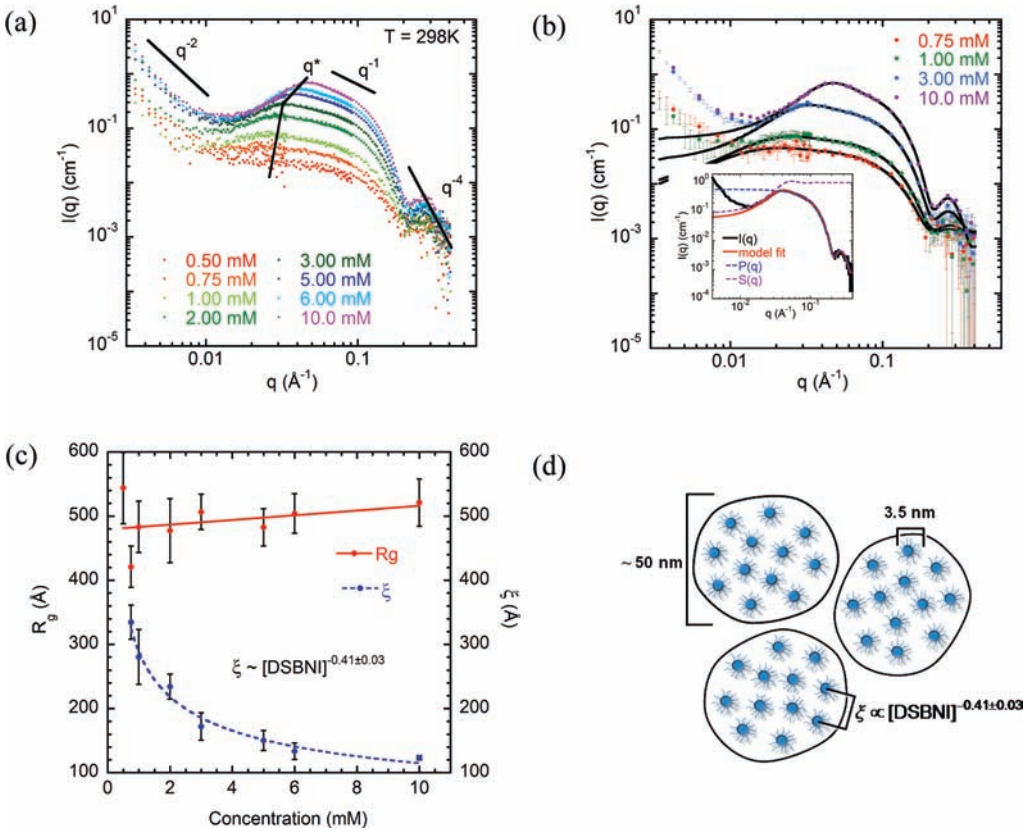

Figure 8. (a) Room temperature (T = 298 K) SANS data of DSBNI aqueous solutions as a function of concentration. All data shown here are obtained at DSBNI concentrations higher than the critical aggregation concentration (CAC). Solid straight lines are drawn to denote −2, −1, and −4 slopes at low, intermediate, and high q regions, respectively. (b) Model fit (solid black lines) to representative data sets using a monodisperse rigid cylinder form factor coupled with screened Coulomb structure factor accounting for the electrostatic repulsions between aggregated structures. Extracted fitting parameters and the goodness of fitting are presented in Table 2. (inset) A representative model fit (for DSBNI conc. 6 mM) deconvoluted into corresponding form and structure factors. (c) Characteristic length scales of the aggregated structure as a function of the DSBNI concentration. The correlation length (ξ) shows a power law behavior relation (scaling exponent -0.41 ± 0.03) with concentration. The length scale corresponding to overall aggregated structure is independent of the concentration and is about 500 Å. (d) A schematic depicting the cross section of the self-assembled structures in aqueous solution as obtained from the SANS analysis.

Table 2. SANS Fitting Parameters Using Cylinder Form Factor and Screened Coulomb Structure Factor[a]

concentration (mM)	volume fraction (φ)	radius (Å)	length (Å)	$(\Delta\rho)^2$ ($\times 10^{-12}$ Å^{-4})	$\lvert z_{\text{eff}} \rvert$	$(\chi^2/n)^{1/2}$
0.50	0.0006	18.2	33.0	18.7	1.9	5.5
0.75	0.0008	18.2	36.4	22.6	2.2	1.4
1.00	0.0009	17.2	38.7	21.6	7.0	1.5
2.00	0.0027	17.6	38.9	20.8	8.8	2.3
3.00	0.0034	17.7	39.8	21.7	9.2	3.7
5.00	0.0066	18.2	37.6	19.8	10.5	3.5
6.00	0.0074	18.2	37.3	21.5	12.9	3.9
10.00	0.0122	18.4	37.5	16.2	23.9	2.6

[a] Attempts to introduce polydispersity into the model using a Flory–Schulz form led to small (<10%) increases in mean cylinder length but did not improve the fits to the data significantly.

plane ("Cylinder B") of the cylinder). To determine which cylinder best represents our data, we fit the SANS of much higher concentration DSBNI (100 mM) (see Supporting Information, S5). The fitting showed that the radius stays constant at 17.77 Å, while the length increased by over 3 times

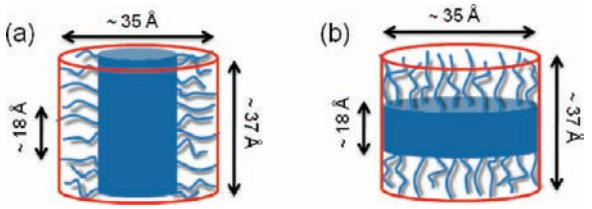

Figure 9. Two possible orientations of DSBNI molecules in the cylinder. In both cases, the solid blue cylinder represents the distyrylbenzene stacks and the whisker-like lines represent the hexyl side chains. From fitting of 100 mM DSBNI, we conclude that Cylinder A shown in (a) best depicts the orientation of the molecules within the aggregates.

to ∼130 Å. Here we conclude that the orientation of the DSBNI molecules can be depicted as shown in "Cylinder A" Figure 9, where chromophores arrange themselves in the radial plane and due to the presence of more DSBNI molecules (in 100 mM conc. solution) associate into the elongated aggregates or longer cylindrical micelles.

The length scale associated with the correlation peak position ($q = q^*$) is a reasonable parameter by which to estimate center to

dx.doi.org/10.1021/ja202776b |J. Am. Chem. Soc. 2011, 133, 8380–8387

center distance between aggregated structures. From a simple first-order approximation, the correlation length ($\xi = 2\pi/q^*$) is expected to depend on DSBNI concentration (or the number of aggregated structures) and the aggregated cylinder diameter at a particular concentration (or the aggregation number). As our model fitting shows that above the CAC, the cylinder diameter (and hence the aggregation number) is independent of concentration, the correlation length (ξ) is primarily a function of the DSBNI concentration or the number of aggregated cylindrical structures.

In Figure 8c, the correlation length is shown as a function of DSBNI concentration. For a spherical structure, the correlation length should vary with the DSBNI concentration through the power law expression: $\xi \sim [\text{DSBNI}]^{-1/3}$.[26,29] On the other hand, for the semidilute regime with cylindrical/rod-like structures, the variation of ξ with concentration should follow: $\xi \sim [\text{DSBNI}]^{-1/2}$.[29,41] Using experimental data, we obtained an intermediate power law exponent of -0.41 ± 0.03. The deviation from the theoretically expected value (-0.5) may arise from the cylinders being extremely short ($r/L = 0.5$), the error associated with the q^* estimation (especially for [DSBNI] < 2 mM), and polydispersity associated with cylinder radius. Further, we mention that several studies, especially regarding polyelectrolyte solutions (in the absence of salt) and charged colloids, reported that q^* scales with polyelectrolyte concentration (c_p) as $c_p^{1/3}$ in the dilute regime (cubic arrangement) and as $c_p^{1/2}$ in the semidilute regime (cylindrical or hexagonal packing).[45−48] The DSBNI concentrations studied here ($1.0 < [\text{DSBNI}]/[\text{DSBNI}]_{CAC} < 20.0$) spans a wide range and may be responsible for such an intermediate scaling relation.

Finally, an upturn in the low q scattering intensity suggests existence of another structural hierarchy associated with this system. We performed Guinier analysis to obtain a crude estimate of the length scale. The Guinier plot is reported in the Supporting Information section (S3 and S4) and the extracted characteristic length scale (R_g) values are plotted against DSBNI concentration in Figure 8c. This characteristic length scale can be conceived as the distance from any cylinder center within which density fluctuation exists (or the density correlation length) and beyond that the system behaves uniformly. The R_g values appeared to be ∼500 Å, and independent of the DSBNI concentration. It is worth mentioning that similar long wavelength concentration fluctuations have previously been documented for other polyelectrolyte and charged colloid systems.[45−50] Further, in this case, the density correlation length scale probably arises from the electrostatic interactions and is quite independent of the concentration, molecular weight (for polyelectrolytes), and temperature.[49] In fact, this length scale is found to be a function of the polymer/micelle charge density.[48] Since all the scattering measurements were performed using D_2O as solvent (i.e., the same solvent dielectric constant) and without presence of any salt, the Debye screening length and the inter cylinder electrostatic interaction is largely conserved here. This reasoning justifies our observation of the concentration independent R_g value. Thus, the self-assembly of DSBNI molecules in aqueous solution can be visualized as represented in Figure 8d. At the lowest structural level, DSBNI molecules organize themselves into cylinders with 35 Å diameter and ∼37 Å length. The mean distance between these cylindrical structures shows a power law relation to DSBNI concentration with a scaling exponent -0.41 ± 0.03. Finally, this assembly is organized within a higher structural order with mean density correlation length of ∼500 Å.

SUMMARY AND CONCLUSION

Both the linear optical properties and TPA spectra of DSBNI in water can be understood on the basis of two concentration regimes: a dilute regime, in which the optical spectra show largely unimolecular characteristics, and a concentrated regime in which intermolecular interactions are dominant.[54] Relevant features upon transition from the low to the high concentration conditions include the hypsochromic PL shift, the increased PL lifetime, the decrease in η, and the increase in TPA cross section. All these changes suggest that the chromophore is exposed to a less polar environment at higher concentrations. The PL blueshift results from a solvatochromic effect in which the less polar environment within the aggregate is less effective at stabilizing the charge-transfer-like excited state. This conclusion is supported by the spectra of the neutral counterpart of DSBNI in nonpolar solvents (1,4-bis(4′-(*N*,*N*-bis(6″-iodohexyl)amino)-styryl)benzene in toluene (λ_{abs} = 409 nm, λ_{PL} = 449 nm).[16] More effective DSBNI—DSBNI contacts lead to interchromophore delocalization and thereby lead to an increase in lifetime and decrease in η.[51−53] Finally, the changes in TPA are more difficult to rationalize succinctly; however, they are consistent with the general trends previously observed as a function of solvent polarity.

Conductance measurements make it possible to estimate the onset of aggregation for DSBNI in pure water at 0.51 mM. Above this concentration, two imaging techniques (liquid AFM and cryo-TEM) and one scattering technique (SANS) indicate that supramolecular structures are formed. Cryo-TEM shows the presence of cylindrical aggregates of ∼400 nm that bundle at high concentrations. With liquid AFM, these aggregates were imaged close to the CAC on a mica surface. The presence of the anionic surface likely facilitates adhesion of the individual cylindrical aggregates. SANS reveals shorter cylindrical micelles in solution. It is clear from a comparison of SANS to liquid AFM that the presence of mica induces propagation of the initial aggregates, elongating the short cylinders to ∼400 nm wormlike structures. Similarly, the wormlike aggregates are only observed in cryo-TEM at a concentration high enough such that is it possible for the shorter micelles to assemble, suggesting that there may be two aggregation threshold concentrations. Finally, SANS shows the presence of short cylindrical micelles in the range of 0.5−10.0 mM. All characterization techniques confirm the cross section to be ∼4 nm and it is apparent that the aggregates exhibit cylindrical architecture in which the long axis of the chromophore lies approximately normal to the micelle propagation vector. We anticipate that other conjugated oligoelectrolytes will exhibit different aggregation threshold values and micellar structures, depending on molecular features such as shape, number of solubilizing groups, and charge density. External influences such as temperature and added electrolytes are also expected to modify the aggregation threshold values and corresponding micellar structures. Altogether, we anticipate that aggregation may be considered as an emerging parameter for modifying optical properties. Furthermore, hydrophobic interactions may be exploited to form nanoscale structures with significant intermolecular π-overlap, which may yield improved charge transport if they can be incorporated within optoelectronic devices.

ASSOCIATED CONTENT

Supporting Information. Details of Guinier analysis and alternate SANS fits; complete citation of ref. 15. This material is available free of charge via the Internet at http://pubs.acs.org.

AUTHOR INFORMATION

Corresponding Author
edkramer@mrl.ucsb.edu; bazan@chem.ucsb.edu

ACKNOWLEDGMENT

The work was supported in part by the National Science Foundation (DMR-1035480) and the Department of Energy (DE-SC0002368). We also acknowledge the support of the National Institute of Standards and Technology, U.S. Department of Commerce, in providing the neutron research facilities used in this work as well as the University of Maryland, NIST Neutron Outreach Travel Grant for small angle neutron scattering (SANS), as well as Dr. Boualem Hammouda and Dr. Steven R. Kline for help with the SANS measurements. Htet Khant is acknowledged for cryo-TEM. T.C. and E.J.K. thank Mitsubishi Chemical Center for Advanced Materials at UCSB for partial support and Prof. Fyl Pincus for useful discussions. We made use of the UCSB MRL Central Facilities funded through the NSF MRSEC Program (DMR 0520415). J.H.O. thanks the UCSB MRL for a travel fellowship and Dr. Nelson Coates for helpful discussions.

REFERENCES

(1) Pinto, M. R.; Schanze, K. S. *Synthesis* **2002**, *9*, 1293–1309.
(2) Hoven, C. V.; Garcia, A.; Bazan, G. C.; Nguyen, T.-Q. *Adv. Mater.* **2008**, *20*, 3793–3810.
(3) Edman, L.; Liu, B.; Vehse, M.; Swensen, J.; Bazan, G. C.; Heeger, A. J. *J. Appl. Phys.* **2005**, *98*, 44502–44510.
(4) Ortony, J. H.; Yang, R. Q.; Brzezinski, J. Z.; Edman, L.; Nguyen, T.-Q.; Bazan, G. C. *Adv. Mater.* **2008**, *20*, 298–302.
(5) Wang, S.; Liu, B.; Gaylord, B. S.; Bazan, G. C. *Adv. Funct. Mater.* **2003**, *13*, 463–467.
(6) Wang, S.; Bazan, G. C. *Adv. Mater.* **2003**, *15*, 1425–1428.
(7) Thomas, S. W.; Joly, G. D.; Swager, T. M. *Chem. Rev.* **2007**, *107*, 1339–1386.
(8) Wang, D.; Gong, X.; Heeger, P. S.; Rininsland, F.; Bazan, G. C.; Heeger, A. J. *Proc. Natl. Acad. Sci. U.S.A.* **2002**, *99*, 49–53.
(9) Garner, L. E.; Park, J.; Dyar, S. M.; Chworos, A.; Sumner, J. J.; Bazan, C. G. *J. Am. Chem. Soc.* **2010**, *132*, 10042–10052.
(10) Yang, R.; Xu, Y.; Dang, X. D.; Nguyen, T. Q.; Cao, Y.; Bazan, G. C. *J. Am. Chem. Soc.* **2008**, *130*, 3282–3283.
(11) Hoven, C.; Yang, R.; Garcia, A.; Heeger, A. J.; Nguyen, T.-Q.; Bazan, G. C. *J. Am. Chem. Soc.* **2007**, *129*, 10976–10977.
(12) Wu, H.; Huang, F.; Mo, Y.; Yang, W.; Wang, D.; Peng, J.; Cao, Y. *Adv. Mater.* **2004**, *16*, 1826–1830.
(13) Nguyen, T.-Q.; Kwong, R. C.; Thompson, M. E.; Schwartz, B. J. *Appl. Phys. Lett.* **2000**, *76*, 2454–2456.
(14) He, G. S.; Tan, L.-S.; Zheng, Q.; Prasad, P. N. *Chem. Rev.* **2008**, *108*, 1245–1330.
(15) Albota, M.; *Science* **1998**, *281*, 1653–1656.
(16) Woo, H. Y.; Liu, B.; Kohler, B.; Korystov, D.; Mikhailovsky, A.; Bazan, G. C. *J. Am. Chem. Soc.* **2005**, *127*, 14721–14729.
(17) Zhao, K.; Ferrighi, L.; Frediani, L.; Wang, C. K.; Luo, Y. *J. Chem. Phys.* **2007**, *126*, 204509–204515.
(18) Hoeben, F. J. M.; Jonkheijm, P.; Meijer, E.; Schenning, A. P. H. J. *Chem. Rev.* **2005**, *105*, 1491–1546.
(19) Brédas, J.; Calbert, J. P.; da Silva Filho, D.; Cornil, J. *Proc. Natl. Acad. Sci. U.S.A.* **2002**, *99*, 5804–5809.
(20) Cornil, J.; Heeger, A.; Brédas, J. *Chem. Phys. Lett.* **1997**, *272*, 463–470.
(21) Collini, E.; Ferrante, C.; Bozio, R. *J. Phys. Chem. B* **2004**, *109*, 2–5.
(22) Xu, C.; Webb, W. W. *J. Opt. Soc. Am. B* **1996**, *13*, 481–491.
(23) Wecksler, S. R.; Mikhailovsky, A.; Korystov, D.; Ford, P. C. *J. Am. Chem. Soc.* **2006**, *128*, 3831–3837.
(24) Becker, W. *Advanced Time-Correlated Single-Photon Counting Techniques*; Springer: Berlin, Heidelberg, NY, 2005.
(25) Kline, S. R. *J. Appl. Crystallogr.* **2006**, *39*, 895–900.
(26) Lee, C. T.; Smith, K. A.; Hatton, T. A. *Langmuir* **2009**, *25*, 13784–13794.
(27) Hayter, J.; Penfold, J. *Mol. Phys.* **1981**, *42*, 109–118.
(28) Hansen, J. P.; Hayter, J. *Mol. Phys.* **1982**, *46*, 651–656.
(29) Chen, S.; Sheu, E. Y.; Kalus, J.; Hoffman, H. *J. Appl. Crystallogr.* **1988**, *21*, 751–769.
(30) Aswal, V. K.; Goyal, P. S. *Phys. Rev. E* **2000**, *61*, 2947–2953.
(31) Cosgrove, T.; White, S. J.; Zarbakhsh, A.; Heenan, R. K.; Howe, A. M. *Langmuir* **1995**, *11*, 744–749.
(32) Hong, J. W.; Woo, H. Y.; Liu, B.; Bazan, G. C. *J. Am. Chem. Soc.* **2005**, *127*, 7435–7443.
(33) Nguyen, T. Q.; Doan, V.; Schwartz, B. J. *J. Chem. Phys.* **1999**, *110*, 4068–4079.
(34) Bartholomew, G. P.; Bazan, G. C. *Acc. Chem. Res.* **2001**, *34*, 30–39.
(35) Treiner, C.; Makayssi, A. *Langmuir* **1992**, *8*, 794–800.
(36) Hansma, P.; Cleveland, J.; Radmacher, M.; Walters, D.; Hillner, P.; Bezanilla, M.; Fritz, M.; Vie, D.; Hansma, H.; Prater, C. *Appl. Phys. Lett.* **1994**, *64*, 1738–1740.
(37) Chworos, A.; Severcan, I.; Koyfman, A. Y.; Weinkam, P.; Oroudjev, E.; Hansma, H. G.; Jaeger, L. *Science* **2004**, *306*, 2068–2072.
(38) Higgins, J. S.; Benoît, H. *Polymers and Neutron Scattering*; Oxford University Press: New York, 1994.
(39) Chen, S. *Annu. Rec. Phys. Chem.* **1986**, *37*, 351–399.
(40) Schmidt, G.; Nakatani, A. I.; Butler, P. D.; Han, C. C. *Macromolecules* **2002**, *35*, 4725–4732.
(41) Chatterjee, T.; Jackson, A.; Krishnamoorti, R. *J. Am. Chem. Soc.* **2008**, *130*, 6934–6935.
(42) Svergun, D. I.; Koch, M. H. J. *Rep. Prog. Phys.* **2003**, *66*, 1735–1782.
(43) Please note that this model (Austin Model 1, AM1) assumes a neutral (total charge zero) closed-shell singlet state of the molecule.
(44) Dewar, M. J. S.; Zoebisch, E. G.; Healy, E. F.; Stewart, J. J. P. *J. Am. Chem. Soc.* **1985**, *107*, 3902–3909.
(45) Borsali, R.; Nguyen, H.; Pecora, R. *Macromolecules* **1998**, *31*, 1548–1555.
(46) Ermi, B. D.; Amis, E. J. *Macromolecules* **1997**, *30*, 6937–6942.
(47) Haro-Pérez, C.; Rojas-Ochoa, L. F.; Castañeda-Priego, R.; Quesada-Pérez, M.; Callejas-Fernández, J.; Hidalgo-Álvarez, R.; Trappe, V. *Phys. Rev. Lett.* **2009**, *102*, 18301–18305.
(48) Zhang, Y.; Douglas, J. F.; Ermi, B. D.; Amis, E. J. *J. Chem. Phys.* **2001**, *114*, 3299–3314.
(49) Ermi, B. D.; Amis, E. J. *Macromolecules* **1998**, *31*, 7378–7384.
(50) Matsuoka, H.; Schwahn, D.; Ise, N. *Macromolecules* **1991**, *24*, 4227–4228.
(51) Birks, J.; Dyson, D.; Munro, I. *Proc. R. Soc. London, Ser. A* **1963**, *275*, 575–588.
(52) Birks, J.; Christophorou, L. *Spectrochim. Acta* **1963**, *19*, 401–410.
(53) Gierschner, J.; Ehni, M.; Egelhaaf, H. J.; Medina, B. M.; Beljonne, D.; Benmansour, H.; Bazan, G. C. *J. Chem. Phys.* **2005**, *123* 144914–144923.
(54) For recent studies on the TPA response of nonemissive organic nanostructures based on porphyrin chromophores, please see: Raymond, J. E; Goodson, T. *J. Phys. Chem. Lett.* **2011**, *2*, 329–333.